In vivo and *in vitro* evaluation of a biodegradable magnesium vascular stent designed by shape optimization strategy

Chenxin Chen[a,b,※], **Jiahui Chen**[c,※], **Wei Wu**[b,d,※], **Yongjuan Shi**[a], **Liang Jin**[a], **Lorenza Petrini**[e], **Li Shen**[c], **Guangyin Yuan**[a,*], **Wenjiang Ding**[a], **Junbo Ge**[c], **Elazer R. Edelman**[f,g], **Francesco Migliavacca**[b,*]

[a]National Engineering Research Center of Light Alloy Net Forming & State Key Laboratory of Metal Matrix Composite, Shanghai Jiao Tong University, 800 Dongchuan Road, Shanghai, China, 200240

[b]Laboratory of Biological Structure Mechanics (LaBS), Department of Chemistry, Materials and Chemical Engineering "Giulio Natta", Politecnico di Milano, Piazza Leonardo da Vinci, 32, Milan, Italy, 20133

[c]Shanghai Institute of Cardiovascular Diseases, Department of Cardiology, Zhongshan Hospital, Fudan University, Shanghai, China, 200032

[d]Department of Mechanical Engineering, The University of Texas at San Antonio, One UTSA Circle, San Antonio, USA, TX 78249-0669

[e]Department of Civil and Environmental Engineering, Politecnico di Milano, Piazza Leonardo da Vinci, 32, Milan, Italy, 20133

[f]Institute for Medical Engineering and Science, Massachusetts Institute of Technology, Cambridge, USA, MA 02139

[g]Cardiovascular Division, Department of Medicine, Brigham and Women 's Hospital, Harvard Medical School, Boston, USA, MA 02115

Abstract

The performance of biodegradable magnesium alloy stents (BMgS) requires special attention to non-uniform residual stress distribution and stress concentration, which can accelerate localized degradation after implantation. We now report on a novel concept in stent shape optimization using a finite element method (FEM) toolkit. A Mg-Nd-Zn-Zr alloy with uniform degradation behavior served as the basis of our BMgS. Comprehensive *in vitro* evaluations drove stent optimization, based on observed crimping and balloon inflation performance, measurement of radial strength, and stress condition validation via microarea-XRD. Moreover, a Rapamycin-eluting polymer coating was sprayed on the prototypical BMgS to improve the corrosion

[*]Corresponding author. gyyuan@sjtu.edu.cn., francesco.migliavacca@polimi.it.
[※]these authors contributed equally to this work.

resistance and release anti-hyperplasia drugs. *In vivo* evaluation of the optimized coated BMgS was conducted in the iliac artery of New Zealand white rabbit with quantitative coronary angiography (QCA), optical coherence tomography (OCT) and micro-CT observation at 1, 3, 5-month follow-ups. Neither thrombus or early restenosis was observed, and the coated BMgS supported the vessel effectively prior to degradation and allowed for arterial healing thereafter.

The proposed shape optimization framework based on FEM provides an novel concept in stent design and in-depth understanding of how deformation history affects the biomechanical performance of BMgS. Computational analysis tools can indeed promote the development of biodegradable magnesium stents.

Graphical Abstract
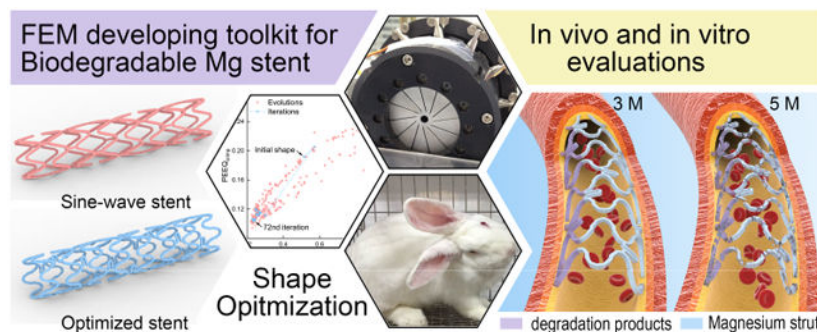
Keywords

shape optimization; finite element method; biodegradable magnesium alloy stent; *in vitro* evaluation; *in vivo* evaluation

1. INTRODUCTION

In the shortest time permanent metallic drug-eluting stent (DES) became the mainstay percutaneous coronary intervention (PCI) revolutionizing the treatment of coronary artery disease (CAD) [1-3]. Yet, they remain for patient lifetimes and impose a rigid limitation to vascular access and arterial vasomotion forever carrying with them the potential late stent thrombosis [4]. To circumvent these issues, bioabsorbable polymeric scaffolds (BRS) and biodegradable magnesium alloy stents (BMgS) were developed, with the idea that they would gradually disappear after providing a arterial healing on par with or superior to DES [5, 6]. The BRS experience has been sobering. While clinical outcomes have been generally non-inferior to DES [7], multiple clinical trials confirmed an increased rate of thrombosis and myocardial infarctions with BRS if anything amplifying over time [8-10]. These results may be partially explained by malapposition from relatively weak polymer BRS materials [11, 12] and asymmetric material degradation from local stress concentration and microstructural damage from stent crimping and implantation [13, 14]. Magnesium alloys offer superior mechanical properties and uniform degradation behavior to polymeric materials [15, 16]. However, they are prone to the same asymmetric strains and degradation introduced by crimp [17, 18].

Computer modeling, including finite-element method (FEM), has become an essential, multifunctional and reliable tool for cardiovascular stents development [19-22]. FEM has been widely employed to assess the biomechanical behavior of cardiovascular stents, in scenarios ranging from idealized simplified geometries to more complex anatomical representation of patient-specific situations [21, 23]. Design optimization can enhance device development and improve the mechanical properties of permanent DES [24-26]. Furthermore, numerical simulations of the behavior of magnesium alloys were established, based on uniform corrosion, phenomenological-stress corrosion mechanism [27], and pitting corrosion [28-30]. Some of the results obtained from numerical simulations were validated via experimental corrosion testing [31, 32]. The slowing of corrosion of BMgS can be achieved via homogenizing the stress distribution with a shape optimization process [33]. An optimization process for BMgS, using adaptive meshing for modeling degradation, improved the stent long-term scaffolding performance [34]. However, crimp deformation was not taken into account in previous shape optimization studies, an effect that may introduce significant plastic deformation, misleading stent designers regarding the *in vivo* stent properties at different timeframes.

Materials properties, structure design and polymer coatings are the three key elements in the development of a BMgS. Corrosion modeling studies of BMgS behavior emphasized that localized corrosion leads to a non-uniform fracture of BMgS, even in an idealized artery geometry [28]. A magnesium alloy with localized corrosion performance can reduce the otherwise excellent biocompatibility, the uniform biodegradability and the adjustable biomechanical properties provided by BMgS [35, 36].

The present study developed a shape optimization framework for BMgS with a generic sine-wave design, made of Mg-2.1Nd-0.2Zn-0.5Zr (JDBM), a magnesium alloy with good mechanical properties and uniform degradation behavior [37]. The shape optimization considering the effect of crimping, was expected to modify the stent deformation history, minimize plastic strains, and homogenize the distribution of residual stresses. Moreover, FEM simulation predictions were verified against *in vitro* experiments. Finally, the optimized BMgS was coated with a Rapamycin eluting polymer and used in an *in vivo* test to proof effectiveness. A polymer coating becomes more critical on BMgS than DES, for anti-proliferative drugs not only reduce initial stenosis, but also prevent early degradation of the magnesium substrate [38, 39].

Together these studies demonstrate the potency of computational modeling in driving device design.

2. MATERIALS AND METHODS

2.1. Study Design

Shape optimization with deformation path control was performed to obtain transform design for a BMgS stent made of JDBM alloy (Figure 1). Systematic *in vitro* experiments and numerical simulations were conducted to evaluate and compare the mechanical performance of the sine-wave and a transformed stent design. The better design was identified and implanted into 12 rabbits' iliac artery to assess biodegradation behavior *in vivo.*

2.2. Shape optimization

Before shape optimization, a topology analysis was carried out for the repeated strut unit of a genetic sine-wave design (SIN stent) to obtain a pre-optimized 2D initial strut design meshed with shell elements. In order to avoid self-contact during crimping, we built the strut mesh based on the inner diameter (2.85 mm) of stent (Figure 2a). The deformation process of the stent included crimping of balloon-mounted stent from initial 3.0 mm (outer diameter) to 1.3 mm, and subsequent stent expansion to 3.2 mm (outer diameter). For shape optimization, the process was simplified to compress and stretch the 2D strut model (Figure 2b, c). Material of JDBM micro-tubes properties manufactured in our previous study [41] were measured in uniaxial tension (Figure 2d). The density of JDBM is 1.84×10^3 kg/m^3, Young's modulus is 45 GPa, Poisson's ratio is 0.35, and isotropic hardening plasticity model is adopted [31]. The morphing method to define the shape domain and variations was reported in our previous research [33]. An algorithm based on global response surface method (GRSM) [42] was applied to control stent shape evolution (Figure 2e). The objective of optimization was to minimize the peak value of equivalent plastic strain on the 2D strut after expansion: $PEEQ_{expand}$. $Spacing_{max}$ and $Spacing_{min}$ were defined as the maximum and minimum values of spacing between the adjacent edges (Figure 2b). We limited the range of $Spacing_{max}$ and $Spacing_{min}$ during optimization iterations to modify the crimped strut shape. Adjacent edges were designed as parallel as possible, to reserve space for polymer drug coating and to avoid self-contact and webbing of coating during crimping. The optimization was formulated as follows:

$$\text{Minimize} \qquad PEEQ_{expand} \qquad (1)$$

$$\text{Subject to} \qquad Spacing_{min} > 0.004\, mm \qquad (2)$$

$$Spacing_{max} < 0.005\, mm \qquad (3)$$

A 3D model was built based on shape optimization (OPT stent) and specimens were manufactured via pulsed laser cutting.

2.3. 3D FEM model

The FEM assembly for 3D simulation was composed of a stent, a folded balloon, a vessel and 12 rigid plates (Figure 1). An 18 mm long balloon with a folded diameter of 1.15 mm and a dilated diameter of 2.70 mm was meshed using 4-nodes quadrilateral membrane elements with reduced integration (M3D4R). A linear elastic model was adopted for the folded balloon, with a density of 1.6×10^3 kg/m^3, Young's modulus of 900 MPa and Poisson's ratio of 0.3. The mock artery dimensions were set to a longitudinal length of 30 mm, inner diameter of 2.8 mm and wall thickness of 1mm. The vessel meshed with C3D8R elements was composed of three layers, i.e., the tunicae intima, media and adventitia, with

respective thicknesses of 0.27, 0.35 and 0.38 mm. The Holzapfel-Gasser-Ogden strain energy potential was used to model the anisotropic behavior of the arterial layers with distributed collagen fiber orientations [43, 44], described by

$$U = C_{10}(\bar{I}_1 - 3) + \frac{k_1}{2k_2}\left(e^{k_2\langle E \rangle^2} - 1\right), \quad (4)$$

$$E = \kappa(\bar{I}_1 - 3) + (1 - 3\kappa)(\bar{I}_4 - 1)$$

where U is the strain energy per unit of reference volume; C_{10}, k_1, k_2 and κ are the material parameters. $\bar{I}_1$ is the first deviatoric strain invariant, $\bar{I}_4$ is the pseudo-invariants of Cauchy-Green deformation tensor, and E represents the deformation of fiber families. The stress-stretch behavior of the three arterial layers was reported by Holzapfel et al [45]. The Holzapfel-Gasser-Ogden strain energy potential applied in artery modeling has been reported by Schiavone et al [46]. The number of elements was 67,344 for the SIN stent, 88,128 for the OPT stent, 16,640 for balloon and 72,000 for the artery, respectively.

Two FEM scenarios, mimicking *in vivo* and *in vitro* test conditions, defined SIN and OPT stents operation and stains, including crimping, expanding and recoil. For the *in vivo* scenario, stents were expanded in an arterial vessel. For the *in vitro* case, stents were expanded freely and then crimped by rigid plates to predict the radial strength. A general contact algorithm was applied to simulate the interaction between plates and stent, balloon and stent as well as vessel and stent, setting a normal hard contact and a tangential behavior with a coefficient of friction of 0.2 [47]. The simulations were run using the ABAQUS/ Explicit code 6.14, (Dassault Systèmes, Vélizy-Villacoublay, France).

2.4. In vitro experimental phase

The SIN and OPT stents were cut out from JDBM micro-tubes of 3 mm of diameter and 160 μm of thickness via pulsed laser, followed by annealing and electrochemical polishing. After electrochemical polishing, the thickness of stent is 150 μm. The stents were crimped on the PTCA balloon catheter with a folded diameter of 1.15 mm and an expanding diameter of 3.0 mm at a nominal pressure of 6 atm (MicroPort Scientific Corporation, Shanghai, China). Inflation was conducted with applied pressure 6 atm under the observation of an optical microscope, and effects on stent dimensions recorded. The dog-boning effect, radial recoil and longitudinal foreshortening were calculated by:

$$\text{dog boning} = \frac{D_{inflating}^{distal} - D_{inflating}^{central}}{D_{inflating}^{distal}} \times 100\% \quad (5)$$

$$\text{radial recoil} = \frac{D^{mean}_{inflating} - D^{mean}_{deflated}}{D^{mean}_{inflating}} \times 100\% \quad (6)$$

$$\text{foreshortening} = \frac{L_{crimped} - L_{deflated}}{L_{crimped}} \times 100\% \quad (7)$$

where $D^{distal}_{inflating}$, $D^{central}_{inflating}$, $D^{mean}_{inflating}$ are the maximum values of the distal diameter central diameter and mean diameter of eight rings during balloon inflating, respectively. $D^{mean}_{deflated}$ and $L_{deflated}$ are the mean diameter and length of stent after deflated the balloon, respectively. $L_{crimped}$ is the length of stent at crimped status [48].

Expanded SIN and OPT stents were re-compressed by the MSI RX500 Radial Force Tester with multi-cycle stepped testing, to calculate radial strength and stiffness. The stent was initially crimped to diameter of 2.8mm, and subsequently unloaded and incrementally reloaded to 2.6, 2.4, 2.2, 2.0 mm sequentially. This pattern is referred to as "multicycle stepped loading" in the ASTM standards [49]. The advantage of this technique is that it allows the plastic deformation to be directly measured at a range of loads. The zero compression diameters, D_0, was the intercept of cycle 1 loading line with the x-axis. The radial stiffness was the slope of cycle 5 loading line. The radial strength was defined as the intercept of radial load curve with a parallel line of cycle 5 loading line starting from $0.9D_0$ at x-axis (10% permanent diameter change from the original size).

2.5. Residual stress measurements

The JDBM stent has a microstructure of equiaxed, recrystallized grains, with a grain size about 10.9 μm [41]. Measurements of residual stress for the stent were carried out in a PROTO LXRD microarea mode, using Cr Kα radiation with an accelerating voltage of 30 kV, a tube current of 30 mA and 100 μm pinholes to reduce the width of the primary beam. The focus on the stent was adjusted by a specially designed dual laser focus. The {104} peak of magnesium at a diffraction angle 2θ ~ 152° was used to determine the stress of the JDBM stent. A lab-made insulated tape stick was inserted in the expanded stent, to assist moving and rotating. Stress determination was performed by:

$$\varepsilon^{\{hkl\}}_{\Phi\Psi} = \frac{1}{2}S^{\{hkl\}}_2[\sigma_{11}sin^2\Psi + \tau_{13}sin(2\Psi)] + S^{\{hkl\}}_1 \quad (8)$$

where $\varepsilon^{\{hkl\}}_{\Phi\Psi}$ is the strain component, $\frac{1}{2}S^{\{hkl\}}_2$ is the X-ray elastic constant of quasi-isotropic material equal to $\frac{1+v}{E^{\{hkl\}}_{eff}}$, σ_{11} is the normal stress component, τ_{13} is the shear stress

component, Ψ is the angle between the specimen surface normal and the scattering vector, $S_1^{\{hkl\}}$ is the X-ray elastic constant of quasi-isotropic material equal to $\frac{-v}{E_{eff}^{\{hkl\}}}$ [50].

2.6. Animal model and surgical procedures

OPT stents were first pre-treated in fluoride acid (40 wt%) for 24 hours to form a protective MgF_2 layer to retard corrosion [51]. A hybrid solution containing poly (lactic-co-glycolic acid) (pLGA) and Rapamycin (RAPA) with an overall solid concentration of 1 w/v% was prepared in ethyl acetate and the mass ratio of RAPA was 12 wt.%. Another solution with a solute concentration of 0.5% w/v% was obtained by dissolving poly (L-lactide-co-trimethylene carbonate) (pLT) in ethyl acetate. Coated OPT stents were prepared using a rotary ultrasonic spray-coating technology to obtain a pLGA/RAPA coating with a drug loading of $1.4 \pm 0.2 \ \mu g/mm^2$ above a pre-sprayed pLT base coating. The stent was then mounted on the angioplasty balloon catheter delivery system (MicroPort Scientific Corporation, Shanghai, China).

The coated OPT stents (n=12) were implanted into the iliac artery of New Zealand white rabbits (weight 3.0-3.5 kg) under digital subtraction angiography (INNOVA2100, GE, USA). All animal experiments were performed according to guidelines approved by the Animal Research Committee of the Zhongshan Hospital, Fudan University (approval number: NSFC 81670319) and following the National Institutes of Health guide for the care and use of Laboratory Animals. Angiography was performed after intra-arterial administration of heparin (100 IU/kg), and the diameter of the iliac artery was measured with quantitative coronary angiography (QCA). The coated OPT stent was deployed in the iliac artery via balloon inflation to 7 atm for 30 seconds. The arteriotomy and dermal layers were sutured after catheter, wire, and sheath removal. All implantation procedures were performed by the same investigator team. Three days before the procedure and throughout the following period, all animals orally received 10 mg Aspirin and 12.5 mg Clopidogrel daily. Serial angiography and the follow-up optical coherence tomography (OCT) were performed to examine the safety and efficiency of the stents. After 1, 3 and 5 months from implantation, stented arteries were harvested. After pressure perfusion with saline to remove blood and immersion fixation in 10% neutral buffered formalin, samples were dehydrated and embedded in methyl methacrylate (MMA). Polished slices (~30 μm thick) from proximal, middle and distal part of each embedded MMA block were stained with haematoxylin-eosin (H&E staining) and visualized by vascular endothelial growth factor (VEGF) and CD68^{+}macrophage immune histology fluorescent (IHF) staining.

2.7. In vivo stent degradation

Micro-computed tomography (micro-CT; Bruker Skyscan 1176, USA) was conducted to analyze the *in vivo* degradation of the stent in the iliac artery of the rabbit. The spatial resolution of micro-CT was 8.7 μm. More specific parameters are shown in Table S1. The residual volumes of internal Mg stent, coating and degradation product were calculated based on the threshold of gray value by the software Mimics (Mimics Research 20.0.lnk, Materialise Co, Ltd, Belgium).

2.8. Statistics and data analysis

Measured experimental results were expressed as the mean ± standard deviations. All tests were performed at least three independent samples for experimental measurements. The results were analyzed via Student's t-test or one-way analysis of variance (ANOVA) using SPSS statistics 19 software (IBM, USA). A confidence level of 95% ($p < 0.05$) was considered statistically significant.

3. RESULTS

3.1. Shape optimization

Stent and strut design were optimized based on the materials properties of JDBM tubes, and the history of iterations. The optimization procedure was driven by GRSM algorithm to match the boundary conditions and converged at an extreme value of $PEEQ_{expand}$ after 72 iterations (Figure 3a). Specially, iterations with the $Spacing_{max}$ below 0.025 mm and $Spacing_{min}$ greater than 0.020 mm were identified. The coordinates in the compressed direction of struts of initial shape and 72nd iteration were shown in Figure 3c. The initial gap between $Spacing_{max}$ and $Spacing_{min}$ (66.38 μm and 22.66 μm) was narrowed to 48.96 μm and 41.66 μm at 72nd iteration. Adjacent edges became almost parallel with sufficient margin to avoid contact. With effective control of crimped shape, both $PEEQ_{expand}$ (the object of the optimization) and $PEEQ_{crimp}$ decreased significantly during the optimization (Figure 3d, e). The laser cutting drawing shows the design details of optimized repeat unit (Figure S1).

3.2. Balloon expansion and dog-boning effect

The differences between SIN and OPT stents were defined using 3D balloon-stent expansion simulations validated by experimental measurements *in vitro* (Figure 4a), including characterization of dog-boning, recoiling and foreshortening (Figure 4b). The deformation of the balloon-stent system calculated by FEM (Figure 4c, e) was highly consistent with experimental results (Figure 4a, d, f). The OPT stent had less dog-boning (22.1±2.1% vs. 28.3±1.3%) and foreshortening in the axial direction (0.6±0.1% vs. 2.7±0.3%) than the SIN stent. Both stents started expanding at proximal and distal ends at a balloon pressure of ~2 atm, achieving an outer diameter of 3.1 mm at 6 atm. In contrast to the SIN stent which was expanded to 2.85±0.18 mm at 4 atm, the OPT stent experienced less dog-boning, obtaining an outer diameter of 2.80±0.24 mm at 3 atm (Figure 4a). Furthermore, non-uniform deformation led to high-stress concentration during expansion. The peak value of maximum principal stress of the SIN stent (308.1 MPa) was higher than the OPT stent (266.4 MPa) at 3 atm, while after full expansion the peak stresses of the SIN and OPT stents fell back to 287.5 MPa and 258.7 MPa at 6 atm (Figure 4c, e), respectively. Both stents had similar recoiling in the radial direction (4.3±0.5% vs. 5.0±0.6%).

3.3. Radial strength and flexibility

Muti-cycle crimping demonstrated that both stents possessed enough stability with deformation to finish the five cycle crimping from 2.8 mm to 2.0 mm (Figure 5a-c). The OPT stent performed 7% lower radial stiffness than the SIN stent (622.1±7.8 vs. 667.4±7.2

kPa/mm). The softer radial stiffness of the OPT stent was coincident with more rapid and uniform expansion with balloon inflation (Figure 4f). The OPT stent also demonstarted 9% higher radial strength (96.7±1.6 vs. 88.8±3.1 kPa). FEM analysis showed the same tendency with experiment results (Figure 5c): OPT stent performed higher radial strength (110.3 kPa vs. 102.1 kPa) and lower sriffness (653.4 kPa/mm vs. 721.5 kPa/mm). A mixed design stent combing optimized repeat unit and the straight connection was simulated for three-point bending test (Figure S2a) based on ASTM-2606 [52]. The result shows that optimized repeat units improve the flexibility of the stent. Moreover, 'n' shape links make the OPT stent more compliant (Figure S2b).

3.4. Residual stress measurement via microarea-XRD

The residual stress measurement position was the symmetry point at the inner edge of bow (indicated by red points and black arrows, Figure 6a, b). Considering the diffraction region is small (100 μm), the limited number of grains results in a great scatter in the $\varepsilon_{\Phi\Psi} - sin^2\Psi$ diagram of {104} planes of magnesium on the stents (Figure 6c, d). Normal residual stresses in the SIN and OPT stent were −53.5±16.4 MPa and −34.9±16.1 MPa while tangential residual stresses were 5.7±7.0 MPa and 24.7±6.9 MPa, respectively.

To compare the residual stress with simulation output directly, force decomposition was based on the cylindrical coordinates (Figure 6a, b), because circumferential and axial stress component is parallel to normal and tangential residual stress respectively. For normal residual stress (Figure 6e, f), the circumferential components at midpoint of the inner edge in SIN and OPT stents were −75.4 MPa and −36.1 MPa respectively. For tangential residual stress (Figure 6g, h), the axial component at same points was 10.6 MPa and 10.7 MPa, within acceptable errors from measured values.

Histograms of maximum principal stresses (Figure 6i) show that the peak stress in SIN stent is higher than in OPT stent (148.7 MPa vs. 124.3MPa), and the volume percentage of high-stress regions (100 MPa) in SIN stent is larger than in OPT stent (4.12% vs. 0.68%) as well. Due to the stress corrosion mechanism, high residual stress regions would be vulnerable in an aggressive solution, like blood plasma.

3.5. Analysis of stress conditions of vascular vessel

Before performing the *in vivo* test, another factor in the selection of the best stent was the non-biological stress exerted to the artery evaluated by FEM. The outer diameter of SIN and OPT stents reached 3.07 and 3.11 mm at inflated state with 7 atm pressure of balloon in the artery, respectively. Compared to free stent expansion, the peak values of maximum principal stress for the SIN and OPT stents respectively increased to 163.3 MPa and 148.0 MPa after being implanted in the arteries (Figure 7a, b).

The radial, circumferential and axial stress components on the intima surface were investigated for the SIN and OPT stents at the end of the balloon inflation. The patterns of the stent cells could be observed in the distributions of radial stress on intima (Figure 7c). The maximum values of circumferential and axial stress for the OPT stents were 53.04 kPa and 21.99 kPa lower but not statistically different from the SIN stent 57.49 kPa and 25.01 kPa, respectively (Figure 7d, e). Similarly von Mises stress on the three layers was lower

with OPT (Figure 9f-h) - peak stresses on the media and the adventitia reached 9.29 kPa and 11.04 kPa for the SIN stent, and 8.87 kPa and 9.51 kPa for the OPT stent. As the stresses on the intima layer were much higher than those on the media and adventitia layers, we calculated the von Mises stress on the surface of intima layer to predict the influences of the SIN and OPT stents (Figure 7i). While the maximum values were 61.62 kPa and 64.16 kPa were without significant difference, it is apparent that the stress distribution on the intima is higher for the SIN than the OPT stent. More specifically, the area fraction of relative high-stress regions (40 kPa) for the SIN and OPT stents were 22.75% and 5.25% respectively. In terms of minimal non-biological stress on vascular vessels, the OPT stent was more suitable than the SIN stent. Considering all the above stent mechanical properties, the OPT stent was chosen in the *in vitro* tests for the implantation into the iliac arteries of rabbits.

3.6. Quantitative coronary angiography and optical coherence tomography

The *in vivo* evaluation, included coronary angiography and optical coherence tomography, at 1, 3 and 5 months follow-up, after implantation of the coated OPT stent in rabbit's iliac artery (Figure 8). The in-scaffold segments were on the right branch of the iliac artery (Figure 8b, h, n), and the luminal diameter distributions were analyzed (Figure 8c, i, o). Neither thrombosis or in-scaffold restenosis were in angiography exams during the treatment period. OCT revealed complete endothelialization and strut embedding into the vessel wall at 1 month post-implantation (Figure 8d-f). The 3-layered appearance of intima, media and adventitia (indicated by the arrows) and fibrous plaques (indicated by the asterisks) demonstrated that the coated OPT stents were biocompatible for vascular vessels. The following OCT observation at 3 months showed that the lumen area increased and the attenuations of signal around the edges of the struts remain sharp (Figure 8j-l), confirming that the OPT stent was intact and efficiently supported the artery wall. Degradation was documented to be present at 5 months, as images were primarily comprised of normal arterial structures and a few calcific plaques (indicated by the double arrows, Figure 8p-r). Furthermore, according to the HE staining results (Figure S3 a and b), the endothelialization of stent was completed and no strut malposition was observed at 1-month post-implantation, which was in line with OCT results. In addition, there were some inflammatory cells, including $CD68^+$ macrophage, to infiltrate in the tissues around strut at 3-months post-implantation (Figure S3 e, f, h), whereas, the infiltration of inflammatory cells attenuated at 5-months post-implantation (Figure S3 i, j, l). Of note, the expression of VEGF, a proangiogenesis cytokine, continuously increased in the tissues around the strut in time-dependent (Figure S3 c, g, k).

The mean-diameters of scaffolded-segments calculated by QCA statistics at post-procedure, 1, 3 and 5 months follow-up were 2.85±0.13, 2.37±0.10, 2.58±0.18 and 2.71±0.23 mm respectively (Figure 9). Endothelialization and neointimal hyperplasia reduced the lumen area during 1 month, while with the sustained scaffolding of OPT stents and vascular physiologic reconstruction, the lumen area increased from 1 month to 5 months follow-up.

3.7. Micro-CT analysis

To obtain the detailed morphology of OPT stents under biodegradation, we performed high-resolution micro-computed tomography scanning of the entire scaffolded-segments vessels

at 1, 3 and 5 months implantation. Reconstructed three-dimensional models of medium contrast regions, corresponding to coating and degradation product, and high contrast kernel, corresponding to internal undegraded magnesium stent, are shown in Figure 10. At 1 month (Figure 10a, b) degradation was not observed as expected. After 3 months, the main structure of the OPT stent remained intact (Figure 10c, d). Proximal and distal rings were subjected to higher contraction force from the adjacent vessels, which accelerated the stress corrosion at the corners of those rings and a few localized fractures initialed there. Finally, as expected, the OPT stent degraded significantly and lost mechanical integrity after 5 months implantation (Figure 10e, f). The volumes of internal magnesium stent after 1, 3 and 5 months implantation are 5.56 ± 0.25, 3.51 ± 0.30, and 2.43 ± 0.35 mm^3, respectively. Nevertheless, the volumes of coating and degradation products at the sequential time points were 1.35 ± 0.02, 1.72 ± 0.09, 1.17 ± 0.14 and 1.28 ± 0.20 mm^3, respectively, maintaining within a stable range. These outcomes revealed that the degradation process was carried out layer by layer from the outside to the inside, a combination of uniform degradation and stress corrosion.

In short, considering the results of *in vivo* evaluation in rabbit iliac artery, coated OPT stent supported vascular vessels effectively during the period prior to degradation post-implantation, and as anticipated began to lose its radial strength gradually with vascular physiologic reconstruction around 5 months.

4. DISCUSSION

In this study, we examined the mechanical response of a magnesium alloy stent of standard sine wave and optimized design. The diameter-pressure response and deformation profiles were highly coincidence between simulation output and experimental observation (Figure 4). Dog-boning effect and longitudinal foreshortening were mitigated significantly after shape optimization (Dog-boning $22.1\pm2.1\%$ vs. $28.3\pm1.3\%$, foreshortening $0.6\pm0.1\%$ vs. $2.7\pm0.3\%$). Radial recoil of the OPT stent, $5.0\pm0.6\%$, matches ISO 25539-2 criterion of 15.0% [53]. Moreover two more interesting results which were not detectable by our experimental study became evident including high stress and large deformation introduced with crimping (SIN 107.4 MPa and OPT 87.5 MPa) and larger stress concentration during inflation than when fully expanded (SIN 308.1 MPa and OPT 266.4 MPa, Figure 4c, e).

Crimping effects have been underestimated in metal stents. While clinical studies indict stress induced by crimping as one of the factors of failure reported for BRS in clinical observations [11, 54], deformation aspects of crimping have rarely been the focus of previous work on cyclical loading of metal stents. It has been assumed that the excellent mechanical properties of the CoCr alloy and permanent implantation negate the effects of crimping, and yet when examined crimping has indeed significantly impacted fracture [13, 14]. Most DES studies of cyclical loading have ignored these issues all together [55, 56]. Crimping effects should be amplified however in devices comprised of far softer and more deformable metals like magnesium alloys, where loads may lead to asymmetric deformation close to the tensile limitation, and increase the fracture risk of BMgS. Thus, the crimping process needs to take into account for the design of BMgS.

Sufficient radial strength is an important factor in maintaining lumen area after stenting. The radial strength value of the OPT stent is almost 10% greater than the SIN stent (96.7±1.6 kPa vs. 88.8±3.1 kPa) under the multicycle loading conditions (Figure 5a, b) recommended by ASTM [49]. With multicycle loading 5 BMgS showed no collapse or buckling (significant drop in diameter without pressure increase), evidence that the collapse pressure of the OPT stent is above 180 kPa (Figure 5b). The collapse pressure of absorbable metal scaffold is reported as 80 kPa (AMS-1; Biotronik AG, Buelach, Switzerland) [18], and 150 kPa for the second generation Mg scaffold (AMS-2; Biotronik AG, Buelach, Switzerland) [6]. Since the loading modes are different, these values can not be compared decirtly. Nevertheless the radial supporting ability of OPT stent looks acceptable. Furthermore, the results showed that the radial stiffness of the OPT stent was a bit lower than SIN stent, which is consistent with the diameter-pressure response during expansion.

Although most of FEM studies of cardiovascular stents report stress distribution, experimental validation is often lacking, for the difficulty or impossibility of conventional measurement techniques given the small size of stents. The recently developed microarea-XRD has been successfully employed to measure the residual stress on CoCr-alloy L-605 stent [57] and 316L stainless steel stent [58]. In the present work, the microarea-XRD method was applied to test the residual stress of BMgS. The residual stress matched the circumferential stress component well for both SIN and OPT stents (Figure 6e, f), which validates, to some extent, the FEM output. Corrosion of BMgS tracks with stress condition [27, 31, 59, 60] and herein comparison of stress distribution was most revealing (Figure 6i). Moreover, we show a significant difference of stress distribution on the vessel for the SIN and OPT stents (Figure 7i). With more uniform expansion (Figure 4a, e, f) the OPT stent had much lower circumferential stress component in the intima surface than the SIN stent (Figure 7d). The 'n-shape' link of the OPT stent almost eliminated the foreshortening in the axial direction(Figure 4b), leading to a much lower axial stress component distribution on vessel compared to the SIN stent(Figure 7e). Stress distribution, especially the high-stress regions, are more uniform in the OPT stent, which may lead to better corrosion resistance *in vivo* and more uniform expansion with less dog-boning effect may reduce coating damage, and the elevated wall stress that may lead to arterial injury [21, 24, 40].

Angiographic and OCT observations of the coated OPT stent in rabbits showed no early thrombosis or intravascular restenosis, reflecting the integrated biocompatibility of the device and its Rapamycin-eluting coating. The pLGA coating retains its integrity after expansion without delamination [40]. Considering that the stents were implanted into health iliac artery of rabbit, the vascular vessel recovered gradually with vessel enlargement in a relatively short period (Figure 8, 9). This finding correlates with positive remodeling, which has been reported to occur between 3 and 6 months by other preclinical studies of BMgS [61]. The detailed morphology of the degraded stent was captured by micro-CT. Based on high-resolution data acquisition and threshold calibration by intact stents (Figure S4), internal Mg stent and degradation production (containing polymer coating) could be distinguished (Figure 10). During the degradation of coated OPT stents, stress corrosion did not crash the supporting structure until 3 months (Figure 11). More important, the lumen increased back to about 95% dimension with the post-implantation, demonstrating vasomotion was restored at 5 months. This outcome is in concert with other clinical reports

and *in vivo* studies of BMgS, degradation at 4 months without any early or later adverse effect via intravascular ultrasound [62], stent-like appearance disappeared at 6 months by OCT and vasomotion was restored [63], re-endothelialization without thrombogenesis or in-stent restenosis [64]. As a comparison with our previous *in vivo* study, bare JDBM stent in rabbit common carotid arteries fractured around 1 month [65], and rapamycin-eluting poly (D, L-lactic acid) coated SIN stent in coronary artery of mini-pig depressed to luminal and failed to support the vessel no more than 2 months [38]. Although this comparison is somewhat coarse, the improvement of the coated OPT stent is still significant.

Materials properties, structure design and polymer coating are the three key elements in the stent design process (Figure 12). Previous study [31, 33] of a magnesium alloy AZ31 stent showed that even a well-designed device could not match the clinical requirements when pitting corrosion was present. In this study, we focused on using a Mg alloy with uniform degradation, Mg-Nd-Zn-Zr. In combination with shape optimization and FEM simulation this new material showed improved mechanical properties and polymer coating properties, bring us closer to requirements of clinical applications. This optimization strategy and numerical toolkit can be applied to BMgS and other biodegradable metals without the serious pitting corrosion seen with zinc alloy.

As with all studies this work must be considered in light of its limitations. We did not consider corrosion during shape optimization. With further research of corrosion mechanism on coated biodegradable alloy and development of computing power, more accurate and comprehensive design optimization strategy will arise. Moreover, devices are anisotropic and the tension-compression asymmetry of Mg alloy may be primary factor accounting for systematic error between the experimental measurements and the simulation results in the radial strength test. Development of a new constitutive equation for specific alloy will improve the accuracy of the FEM simulations. Thirdly, the vascular vessel in this study was based on idealized geometries. *In vivo* imaging, and animal- or patient-specific artery geometries will contribute to more instructive information outputs. Finally, microarea-XRD was limited by the X-ray attenuation coefficient of magnesium, the grain size and the diameter of the pinhole in the equipment. Observation of the deformation history via the digital image correlation may be an alternative plan.

5. CONCLUSIONS

This study provides a robust shape optimization framework and development tool for biodegradable magnesium stents. The main findings for the design methodology of BMgS are summarized as follows:

1. Because of the large deformation introduced by crimping and high stress of stents during implantation, the complete deformation history of BMgS should be considered.

2. Shape optimization with deformation history controlling could modify the crimped shape of BMgS, leading to parallel adjacent edges and improving the biomechanical behavior significantly.

3. Finite element model could calculate reliable and precise balloon inflation profiles and stress distribution of the stents. However, the experimental measurement of radial strength is indispensable, especially the multicycle stepped loading method.

4. Numerical simulation of the interaction between the stent and the vascular vessel could provide instructive information for the clinician before device implantation.

Furthermore, an optimized Mg-Nd-Zn-Zr stent was developed via our framework and was comprehensively evaluated *in vitro* and *in vivo*. The key improvements are summarized as follows:

1. The mechanical properties of BMgS were enhanced by design optimization compared to SIN stent, resulting in dog-boning effect (22.1% to 28.3%), longitudinal foreshortening (0.6% to 2.7%) and radial strength (96.7 kPa to 88.8 kPa).

2. With the design optimization, the percentage of high-stress regions of stent (4.12% to 0.68%) and vascular vessel (22.75% to 5.25%) was decreased.

3. Rapamycin eluting coating OPT stents exhibit suitable biocompatibility and unfailing support ability to vessel no less than three months, besides the vasomotion was restored at five months.

Supplementary Material

Refer to Web version on PubMed Central for supplementary material.

ACKNOWLEDGMENTS

REFERENCES

[1]. Stefanini GG, Holmes DR Jr., Drug-eluting coronary-artery stents, N Engl J Med 368(3) (2013) 254–265. [PubMed: 23323902]

[2]. Palmerini T, Benedetto U, Biondi-Zoccai G, Della Riva D, Bacchi-Reggiani L, Smits PC, Vlachojannis GJ, Jensen LO, Christiansen EH, Berencsi K, Valgimigli M, Orlandi C, Petrou M, Rapezzi C, Stone GW, Long-Term Safety of Drug-Eluting and Bare-Metal Stents: Evidence From a Comprehensive Network Meta-Analysis, J Am Coll Cardiol 65(23) (2015) 2496–2507. [PubMed: 26065988]

[3]. Collet C, Capodanno D, Onuma Y, Banning A, Stone GW, Taggart DP, Sabik J, Serruys PW, Left main coronary artery disease: pathophysiology, diagnosis, and treatment, Nat Rev Cardiol 15(6) (2018) 321–331. [PubMed: 29599504]

[4]. Ong DS, Jang IK, Causes, assessment, and treatment of stent thrombosis--intravascular imaging insights, Nat Rev Cardiol 12(6) (2015) 325–336. [PubMed: 25781415]

[5]. Bangalore S, Bezerra HG, Rizik DG, Armstrong EJ, Samuels B, Naidu SS, Grines CL, Foster MT, Choi JW, Bertolet BD, Shah AP, Torguson R, Avula SB, Wang JC, Zidar JP, Maksoud A, Kalyanasundaram A, Yakubov SJ, Chehab BM, Spaedy AJ, Potluri SP, Caputo RP, Kondur A,

Merritt RF, Kaki A, Quesada R, Parikh MA, Toma C, Matar F, DeGregorio J, Nicholson W, Batchelor W, Gollapudi R, Korngold E, Sumar R, Chrysant GS, Li J, Gordon JB, Dave RM, Attizzani GF, Stys TP, Gigliotti OS, Murphy BE, Ellis SG, Waksman R, The State of the Absorb Bioresorbable Scaffold: Consensus From an Expert Panel, JACC. Cardiovascular interventions 10(23) (2017) 2349–2359. [PubMed: 29216997]

[6]. Im SH, Jung Y, Kim SH, Current status and future direction of biodegradable metallic and polymeric vascular scaffolds for next-generation stents, Acta Biomater 60 (2017) 3–22. [PubMed: 28716610]

[7]. Wykrzykowska JJ, Kraak RP, Hofma SH, van der Schaaf RJ, Arkenbout EK, AJ IJ, Elias J, van Dongen IM, Tijssen RYG, Koch KT, Baan J Jr., Vis MM, de Winter RJ, Piek JJ, Tijssen JGP, Henriques JPS, A. Investigators, Bioresorbable Scaffolds versus Metallic Stents in Routine PCI, N Engl J Med 376(24) (2017) 2319–2328. [PubMed: 28402237]

[8]. Ali ZA, Serruys PW, Kimura T, Gao R, Ellis SG, Kereiakes DJ, Onuma Y, Simonton C, Zhang Z, Stone GW, 2-year outcomes with the Absorb bioresorbable scaffold for treatment of coronary artery disease: a systematic review and meta-analysis of seven randomised trials with an individual patient data substudy, Lancet 390(10096) (2017) 760–772. [PubMed: 28732815]

[9]. Kereiakes DJ, Ellis SG, Metzger C, Caputo RP, Rizik DG, Teirstein PS, Litt MR, Kini A, Kabour A, Marx SO, Popma JJ, McGreevy R, Zhang Z, Simonton C, Stone GW, A.I. Investigators, 3-Year Clinical Outcomes With Everolimus-Eluting Bioresorbable Coronary Scaffolds: The ABSORB III Trial, J Am Coll Cardiol 70(23) (2017) 2852–2862. [PubMed: 29100702]

[10]. Moriyama N, Shishido K, Tanaka Y, Yokota S, Hayashi T, Miyashita H, Koike T, Yokoyama H, Takada T, Nishimoto T, Ochiai T, Tobita K, Yamanaka F, Mizuno S, Murakami M, Takahashi S, Saito S, Neoatherosclerosis 5 Years After Bioresorbable Vascular Scaffold Implantation, J Am Coll Cardiol 71(17) (2018) 1882–1893. [PubMed: 29699614]

[11]. Yamaji K, Ueki Y, Souteyrand G, Daemen J, Wiebe J, Nef H, Adriaenssens T, Loh JP, Lattuca B, Wykrzykowska JJ, Gomez-Lara J, Timmers L, Motreff P, Hoppmann P, Abdel-Wahab M, Byrne RA, Meincke F, Boeder N, Honton B, O'Sullivan CJ, Ielasi A, Delarche N, Christ G, Lee JKT, Lee M, Amabile N, Karagiannis A, Windecker S, Raber L, Mechanisms of Very Late Bioresorbable Scaffold Thrombosis: The INVEST Registry, J Am Coll Cardiol 70(19) (2017) 2330–2344. [PubMed: 29096803]

[12]. Jinnouchi H, Torii S, Sakamoto A, Kolodgie FD, Virmani R, Finn AV, Fully bioresorbable vascular scaffolds: lessons learned and future directions, Nat Rev Cardiol 16(5) (2019) 286–304. [PubMed: 30546115]

[13]. Wang PJ, Ferralis N, Conway C, Grossman JC, Edelman ER, Strain-induced accelerated asymmetric spatial degradation of polymeric vascular scaffolds, Proc Natl Acad Sci U S A 115(11) (2018) 2640–2645. [PubMed: 29483243]

[14]. Wang PJ, Nezami FR, Gorji MB, Berti F, Petrini L, Wierzbicki T, Migliavacca F, Edelman ER, Effect of working environment and procedural strategies on mechanical performance of bioresorbable vascular scaffolds, Acta Biomater 82 (2018) 34–43. [PubMed: 30342288]

[15]. Zheng YF, Gu XN, Witte F, Biodegradable metals, Materials Science and Engineering: R: Reports 77(0) (2014) 1–34.

[16]. Bowen PK, Shearier ER, Zhao S, Guillory RJ 2nd, Zhao F, Goldman J, Drelich JW, Biodegradable Metals for Cardiovascular Stents: from Clinical Concerns to Recent Zn-Alloys, Adv Healthc Mater 5(10) (2016) 1121–1140. [PubMed: 27094868]

[17]. Haude M, Erbel R, Erne P, Verheye S, Degen H, Bose D, Vermeersch P, Wijnbergen I, Weissman N, Prati F, Waksman R, Koolen J, Safety and performance of the drug-eluting absorbable metal scaffold (DREAMS) in patients with de-novo coronary lesions: 12 month results of the prospective, multicentre, first-in-man BIOSOLVE-I trial, Lancet 381(9869) (2013) 836–844. [PubMed: 23332165]

[18]. Erbel R, Di Mario C, Bartunek J, Bonnier J, de Bruyne B, Eberli FR, Erne P, Haude M, Heublein B, Horrigan M, Ilsley C, Bose D, Koolen J, Luscher TF, Weissman N, Waksman R, P.-A. Investigators Temporary scaffolding of coronary arteries with bioabsorbable magnesium stents: a prospective, non-randomised multicentre trial, Lancet 369(9576) (2007) 1869–1875. [PubMed: 17544767]

[19]. Darnell M, Mooney DJ, Leveraging advances in biology to design biomaterials, Nat Mater 16(12) (2017) 1178–1185. [PubMed: 29170558]

[20]. Karanasiou GS, Papafaklis MI, Conway C, Michalis LK, Tzafriri R, Edelman ER, Fotiadis DI, Stents: Biomechanics, Biomaterials, and Insights from Computational Modeling, Ann Biomed Eng 45(4) (2017) 853–872. [PubMed: 28160103]

[21]. Antoniadis AP, Mortier P, Kassab G, Dubini G, Foin N, Murasato Y, Giannopoulos AA, Tu S, Iwasaki K, Hikichi Y, Migliavacca F, Chiastra C, Wentzel JJ, Gijsen F, Reiber JH, Barlis P, Serruys PW, Bhatt DL, Stankovic G, Edelman ER, Giannoglou GD, Louvard Y, Chatzizisis YS, Biomechanical Modeling to Improve Coronary Artery Bifurcation Stenting: Expert Review Document on Techniques and Clinical Implementation, JACC. Cardiovascular interventions 8(10) (2015) 1281–96. [PubMed: 26315731]

[22]. Morris PD, Iqbal J, Chiastra C, Wu W, Migliavacca F, Gunn JP, Simultaneous kissing stents to treat unprotected left main stem coronary artery bifurcation disease; stent expansion, vessel injury, hemodynamics, tissue healing, restenosis, and repeat revascularization, Catheter Cardiovasc Interv 92(6) (2018) E381–E392. [PubMed: 29693768]

[23]. Sweeney CA, O'Brien B, McHugh PE, Leen SB, Experimental characterisation for micromechanical modelling of CoCr stent fatigue, Biomaterials 35(1) (2014) 36–48. [PubMed: 24120042]

[24]. Pant S, Limbert G, Curzen NP, Bressloff NW, Multiobjective design optimisation of coronary stents, Biomaterials 32(31) (2011) 7755–7773. [PubMed: 21821283]

[25]. Bressloff NW, Ragkousis G, Curzen N, Design Optimisation of Coronary Artery Stent Systems, Ann Biomed Eng 44(2) (2016) 357–367. [PubMed: 26183960]

[26]. Conway C, McGarry JP, Edelman ER, McHugh PE, Numerical Simulation of Stent Angioplasty with Predilation: An Investigation into Lesion Constitutive Representation and Calcification Influence, Ann Biomed Eng 45(9) (2017) 2244–2252. [PubMed: 28488215]

[27]. Gastaldi D, Sassi V, Petrini L, Vedani M, Trasatti S, Migliavacca F, Continuum damage model for bioresorbable magnesium alloy devices - Application to coronary stents, J Mech Behav Biomed Mater 4(3) (2011) 352–365. [PubMed: 21316623]

[28]. Grogan JA, O'Brien BJ, Leen SB, McHugh PE, A corrosion model for bioabsorbable metallic stents, Acta Biomaterialia 7(9) (2011) 3523–3533. [PubMed: 21664498]

[29]. Grogan JA, Leen SB, McHugh PE, A physical corrosion model for bioabsorbable metal stents, Acta Biomaterialia 10(5) (2014) 2313–2322. [PubMed: 24412771]

[30]. Debusschere N, Segers P, Dubruel P, Verhegghe B, De Beule M, A Computational Framework to Model Degradation of Biocorrodible Metal Stents Using an Implicit Finite Element Solver, Ann Biomed Eng 44(2) (2016) 382–390. [PubMed: 26703421]

[31]. Wu W, Chen S, Gastaldi D, Petrini L, Mantovani D, Yang K, Tan L, Migliavacca F, Experimental data confirm numerical modeling of the degradation process of magnesium alloys stents, Acta Biomater 9(10) (2013) 8730–8739. [PubMed: 23128160]

[32]. Boland EL, Shirazi RN, Grogan JA, McHugh PE, Mechanical and Corrosion Testing of Magnesium WE43 Specimens for Pitting Corrosion Model Calibration, Advanced Engineering Materials 20(10) (2018).

[33]. Wu W, Petrini L, Gastaldi D, Villa T, Vedani M, Lesma E, Previtali B, Migliavacca F, Finite element shape optimization for biodegradable magnesium alloy stents, Ann Biomed Eng 38(9) (2010) 2829–2840. [PubMed: 20446037]

[34]. Grogan JA, Leen SB, McHugh PE, Optimizing the design of a bioabsorbable metal stent using computer simulation methods, Biomaterials 34(33) (2013) 8049–8060. [PubMed: 23906516]

[35]. Willbold E, Gu X, Albert D, Kalla K, Bobe K, Brauneis M, Janning C, Nellesen J, Czayka W, Tillmann W, Zheng Y, Witte F, Effect of the addition of low rare earth elements (lanthanum, neodymium, cerium) on the biodegradation and biocompatibility of magnesium, Acta Biomater 11 (2015) 554–562. [PubMed: 25278442]

[36]. Li X, Liu X, Wu S, Yeung KWK, Zheng Y, Chu PK, Design of magnesium alloys with controllable degradation for biomedical implants: From bulk to surface, Acta Biomater 45 (2016) 2–30. [PubMed: 27612959]

[37]. Mao L, Shen L, Niu J, Zhang J, Ding W, Wu Y, Fan R, Yuan G, Nanophasic biodegradation enhances the durability and biocompatibility of magnesium alloys for the next-generation vascular stents, Nanoscale 5(20) (2013) 9517–9522. [PubMed: 23989064]

[38]. Shi YJ, Zhang L, Chen J, Zhang J, Yuan F, Shen L, Chen C, Pei J, Li Z, Tan J, Yuan G, In vitro and in vivo degradation of rapamycin-eluting Mg-Nd-Zn-Zr alloy stents in porcine coronary arteries, Mater Sci Eng C Mater Biol Appl 80 (2017) 1–6. [PubMed: 28866142]

[39]. Yang Z, Yang Y, Zhang L, Xiong K, Li X, Zhang F, Wang J, Zhao X, Huang N, Mussel-inspired catalytic selenocystamine-dopamine coatings for long-term generation of therapeutic gas on cardiovascular stents, Biomaterials 178 (2018) 1–10. [PubMed: 29902532]

[40]. Chen CX, Tan JY, Wu W, Petrini L, Zhang L, Shi YJ, Cattarinuzzi E, Pei J, Huang H, Ding WJ, Yuan GY, Migliavacca F, Modeling and Experimental Studies of Coating Delamination of Biodegradable Magnesium Alloy Cardiovascular Stents, Acs Biomaterials Science & Engineering 4(11) (2018) 3864–3873.

[41]. Liu F, Chen C, Niu J, Pei J, Zhang H, Huang H, Yuan G, The processing of Mg alloy micro-tubes for biodegradable vascular stents, Mater Sci Eng C Mater Biol Appl 48 (2015) 400–407. [PubMed: 25579940]

[42]. Sobester A, Leary SJ, Keane AJ, On the design of optimization strategies based on global response surface approximation models, Journal of Global Optimization 33(1) (2005) 31–59.

[43]. Holzapfel GA, Gasser TC, Ogden RW, A new constitutive framework for arterial wall mechanics and a comparative study of material models, Journal of Elasticity 61(1-3) (2000) 1–48.

[44]. Gasser TC, Ogden RW, Holzapfel GA, Hyperelastic modelling of arterial layers with distributed collagen fibre orientations, J R Soc Interface 3(6) (2006) 15–35. [PubMed: 16849214]

[45]. Holzapfel GA, Sommer G, Gasser CT, Regitnig P, Determination of layer-specific mechanical properties of human coronary arteries with nonatherosclerotic intimal thickening and related constitutive modeling, Am J Physiol Heart Circ Physiol 289(5) (2005) 2048–2058.

[46]. Schiavone A, Zhao LG, A computational study of stent performance by considering vessel anisotropy and residual stresses, Mater Sci Eng C Mater Biol Appl 62 (2016) 307–16. [PubMed: 26952428]

[47]. Conway C, McGarry JP, McHugh PE, Modelling of atherosclerotic plaque for use in a computational test-bed for stent angioplasty, Ann Biomed Eng 42(12) (2014) 2425–39. [PubMed: 25209735]

[48]. ASTM, F2079-09 Standard Test Method for Measuring Intrinsic Elastic Recoil of Balloon-Expandable Stents, 2013.

[49]. ASTM, F3067-14 Radial Loading of Balloon Expandable and Self Expanding Vascular Stents, 2014.

[50]. ASTM, E2860-12 Standard Test Method for Residual Stress Measurement by X-Ray Diffraction for Bearing Steels, 2012.

[51]. Shi YJ, Pei J, Zhang L, Lee BK, Yun Y, Zhang J, Li ZH, Gu S, Park K, Yuan GY, Understanding the effect of magnesium degradation on drug release and anti-proliferation on smooth muscle cells for magnesium-based drug eluting stents, Corrosion Science 123 (2017) 297–309.

[52]. ASTM, F2606-08 Three-Point Bending of Balloon Expandable Vascular Stents and Stent Systems, 2014.

[53]. I. 25539-2, Cardiovascular implants—endovascular devices—part 2: vascular stents, 2012.

[54]. Ge J, Bioresorbable vascular scaffold for the treatment of coronary in-stent restenosis: New dawn or frost on snow?, Catheter Cardiovasc Interv 92(4) (2018) 678–679. [PubMed: 30341828]

[55]. Petrini L, Trotta A, Dordoni E, Migliavacca F, Dubini G, Lawford PV, Gosai JN, Ryan DM, Testi D, Pennati G, A Computational Approach for the Prediction of Fatigue Behaviour in Peripheral Stents: Application to a Clinical Case, Annals of Biomedical Engineering 44(2) (2016) 536–547. [PubMed: 26433586]

[56]. Morlacchi S, Pennati G, Petrini L, Dubini G, Migliavacca F, Influence of plaque calcifications on coronary stent fracture: a numerical fatigue life analysis including cardiac wall movement, J Biomech 47(4) (2014) 899–907. [PubMed: 24468208]

[57]. Kowalski W, Dammer M, Bakczewitz F, Schmitz KP, Grabow N, Kessler O, In-situ investigation of stress conditions during expansion of bare metal stents and PLLA-coated stents using the XRD sin(2)psi-technique, J Mech Behav Biomed Mater 49 (2015) 23–29. [PubMed: 25974098]

[58]. Liang C, Hu Y, Wang H, Xia D, Li Q, Zhang J, Yang J, Li B, Li H, Han D, Dong M, Biomimetic cardiovascular stents for in vivo re-endothelialization, Biomaterials 103 (2016) 170–182. [PubMed: 27380443]

[59]. Galvin E, Cummins C, Yoshihara S, Mac Donald BJ, Lally C, Plastic strains during stent deployment have a critical influence on the rate of corrosion in absorbable magnesium stents, Med Biol Eng Comput 55(8) (2017) 1261–1275. [PubMed: 27785607]

[60]. Zheng Y, Li Y, Chen JH, Zou ZY, Effects of tensile and compressive deformation on corrosion behaviour of a Mg-Zn alloy, Corrosion Science 90 (2015) 445–450.

[61]. Iqbal J, Onuma Y, Ormiston J, Abizaid A, Waksman R, Serruys P, Bioresorbable scaffolds: rationale, current status, challenges, and future, Eur Heart J 35(12) (2014) 765–776. [PubMed: 24366915]

[62]. Waksman R, Erbel R, Di Mario C, Bartunek J, de Bruyne B, Eberli FR, Erne P, Haude M, Horrigan M, Ilsley C, Bose D, Bonnier H, Koolen J, Luscher TF, Weissman NJ, P.-A. Investigators, Early- and long-term intravascular ultrasound and angiographic findings after bioabsorbable magnesium stent implantation in human coronary arteries, JACC. Cardiovascular interventions 2(4) (2009) 312–320. [PubMed: 19463443]

[63]. Haude M, Ince H, Abizaid A, Toelg R, Lemos PA, von Birgelen C, Christiansen EH, Wijns W, Neumann FJ, Kaiser C, Eeckhout E, Lim ST, Escaned J, Garcia-Garcia HM, Waksman R, Safety and performance of the second-generation drug-eluting absorbable metal scaffold in patients with de-novo coronary artery lesions (BIOSOLVE-II): 6 month results of a prospective, multicentre, non-randomised, first-in-man trial, Lancet 387(10013) (2016) 31–39. [PubMed: 26470647]

[64]. Liu J, Zheng B, Wang P, Wang X, Zhang B, Shi Q, Xi T, Chen M, Guan S, Enhanced in Vitro and in Vivo Performance of Mg-Zn-Y-Nd Alloy Achieved with APTES Pretreatment for Drug-Eluting Vascular Stent Application, ACS Appl Mater Interfaces 8(28) (2016) 17842–17858. [PubMed: 27331417]

[65]. Zhang J, Li H, Wang W, Huang H, Pei J, Qu H, Yuan G, Li Y, The degradation and transport mechanism of a Mg-Nd-Zn-Zr stent in rabbit common carotid artery: A 20-month study, Acta Biomater 69 (2018) 372–384. [PubMed: 29369807]
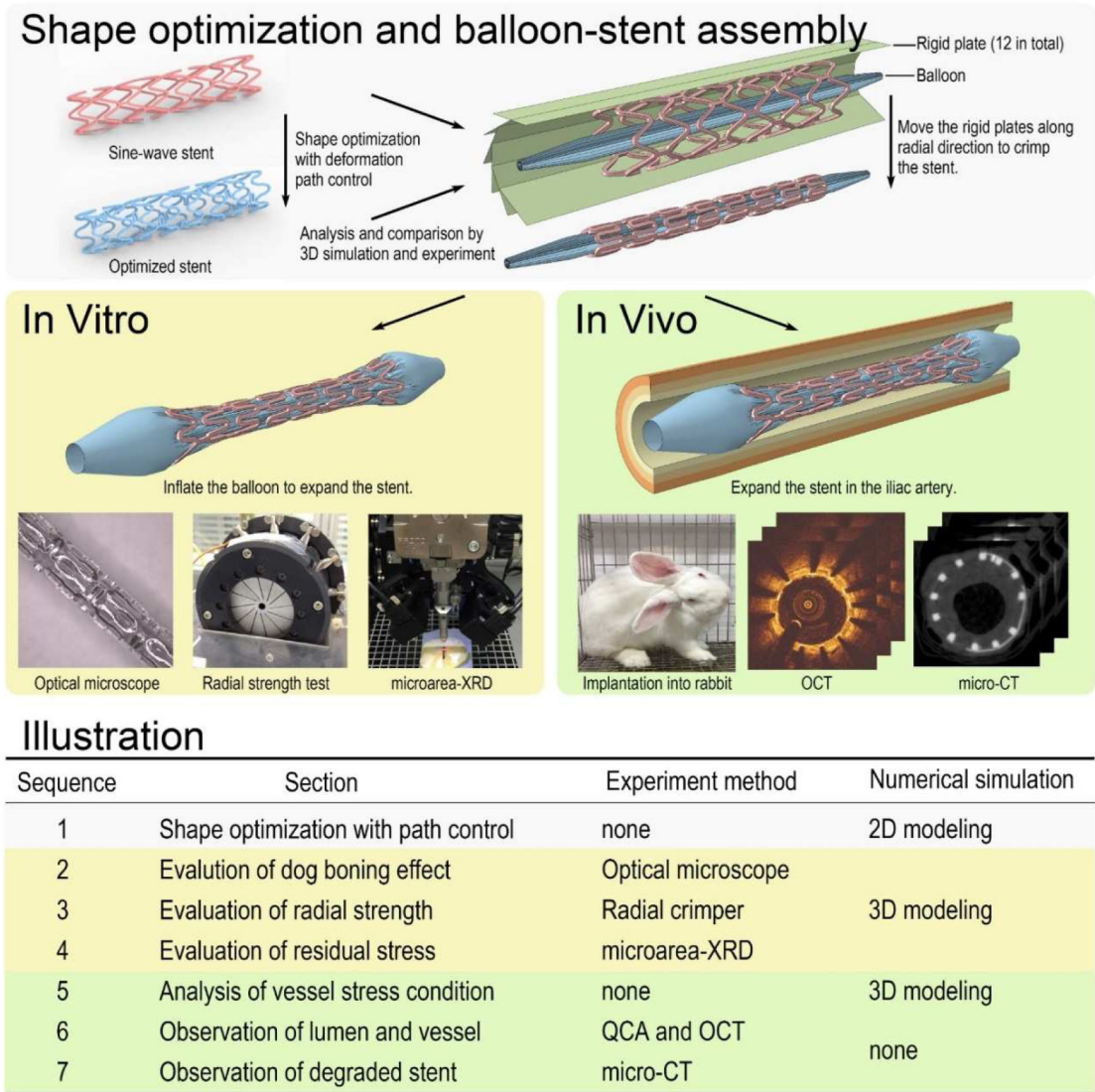
Shape optimization and balloon-stent assembly

Sine-wave stent → Shape optimization with deformation path control → Optimized stent

Analysis and comparison by 3D simulation and experiment

— Rigid plate (12 in total)
— Balloon

Move the rigid plates along radial direction to crimp the stent.

In Vitro

Inflate the balloon to expand the stent.

Optical microscope | Radial strength test | microarea-XRD

In Vivo

Expand the stent in the iliac artery.

Implantation into rabbit | OCT | micro-CT

Illustration

Sequence	Section	Experiment method	Numerical simulation
1	Shape optimization with path control	none	2D modeling
2	Evalution of dog boning effect	Optical microscope	3D modeling
3	Evaluation of radial strength	Radial crimper	
4	Evaluation of residual stress	microarea-XRD	
5	Analysis of vessel stress condition	none	3D modeling
6	Observation of lumen and vessel	QCA and OCT	none
7	Observation of degraded stent	micro-CT	

Figure 1.
Study flowchart. Device optimization morphed a sine-wave ring stent with a 6 crown and open-cell structure into an enhanced design. Detailed structure parameters were extracted from previous studies [40].
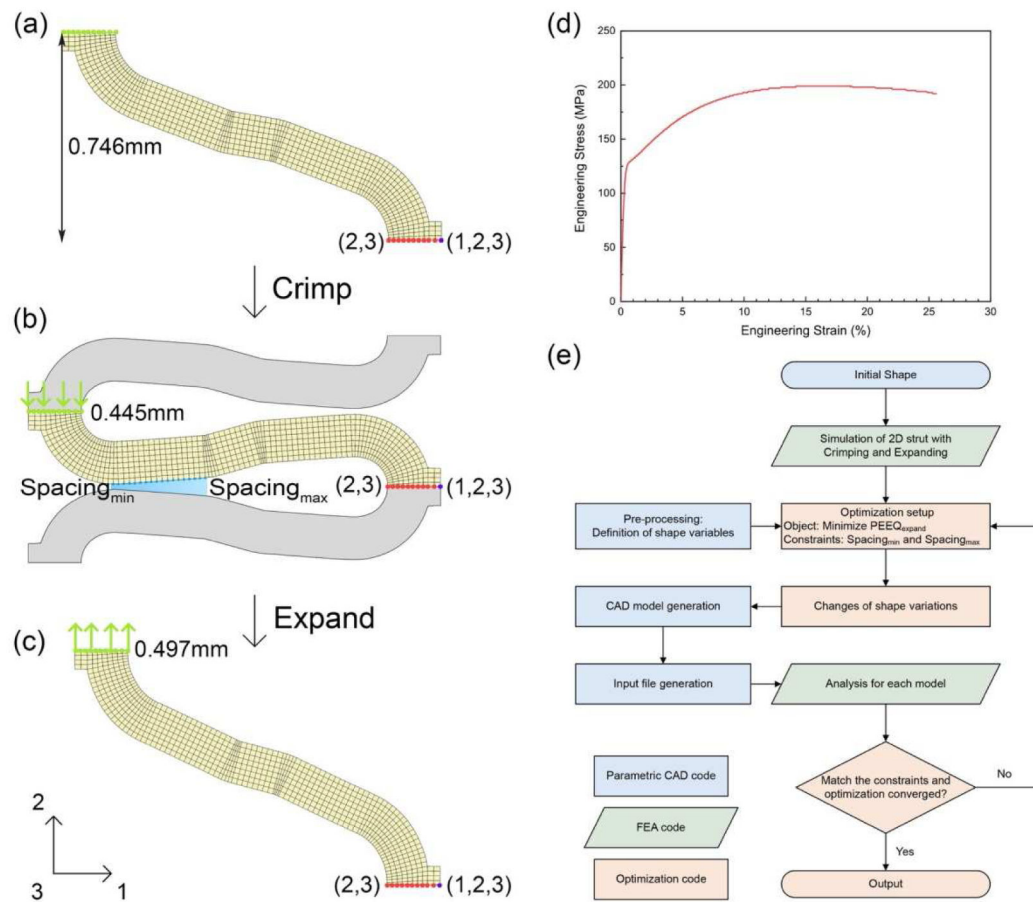
Figure 2.
The boundary conditions and displacement loadings for the 2D strut model during shape morphing program. (a) The 2D initial shape (b) the crimped status and (c) the expanded status. The spacing values were introduced to modify the shape of the adjacent borders of the crimped strut. (d) The engineering stress-strain curve of JDBM used for manufacturing the cardiovascular stents. (e) The flow chart of the shape optimization procedure for the 2D strut model.
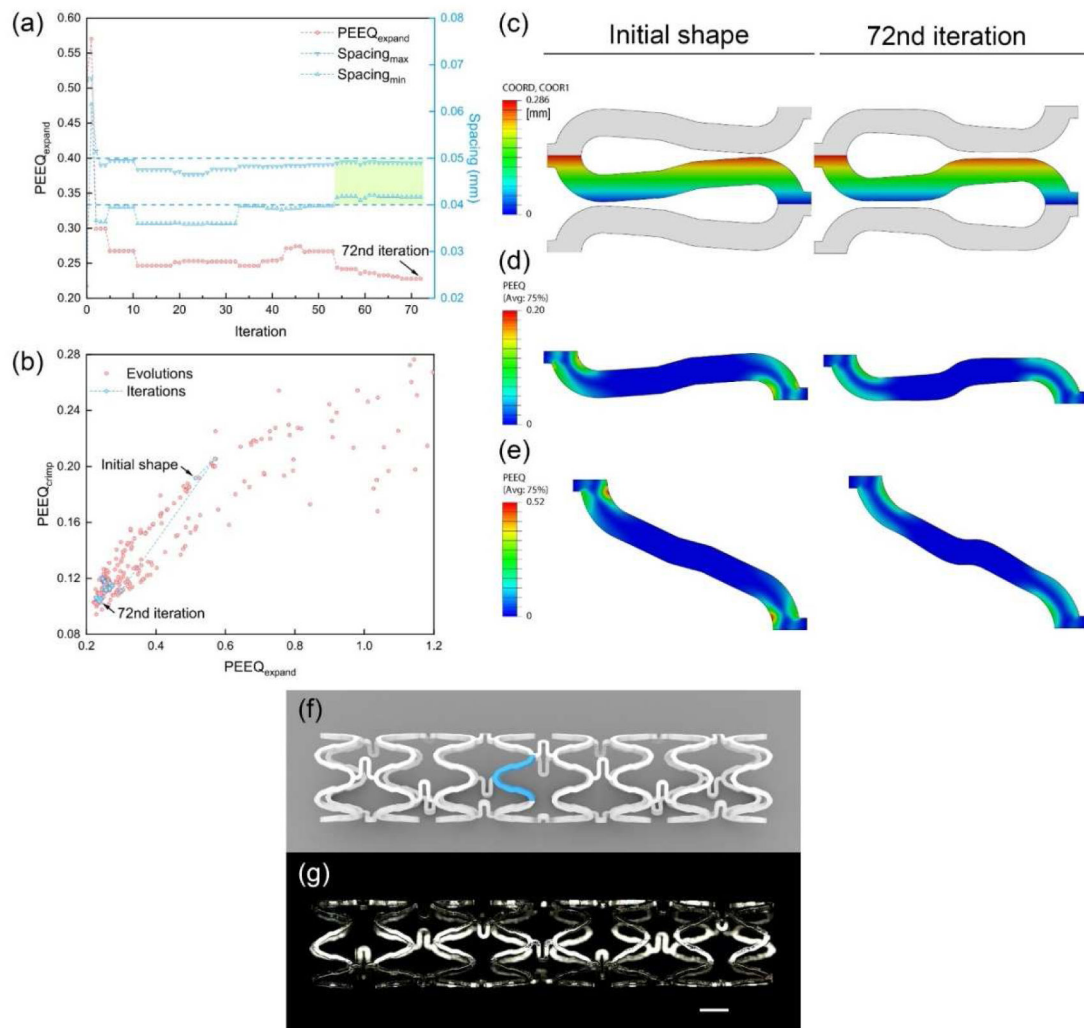
Figure 3.
Shape optimization based on 2D strut model. (a) Optimization history of the maximum equivalent plastic strain after expanding ($PEEQ_{expand}$) and range of spacing between adjacent strut edges after crimping ($Spacing_{max}$ and $Spacing_{min}$). The results matching the boundary conditions of spacing were shaded for distinction. (b) $PEEQ_{crimp}$ versus $PEEQ_{expand}$ plots of attempt evolutions and selected output of each iterations. (c) The strut coordinates in compress direction for initial and optimized shape. (d, e) The distributions of PEEQ for initial and optimized shapes after crimping and expanding. (f, g) The 3D model and the manufactured optimized stent (scale bar represents 1 mm).
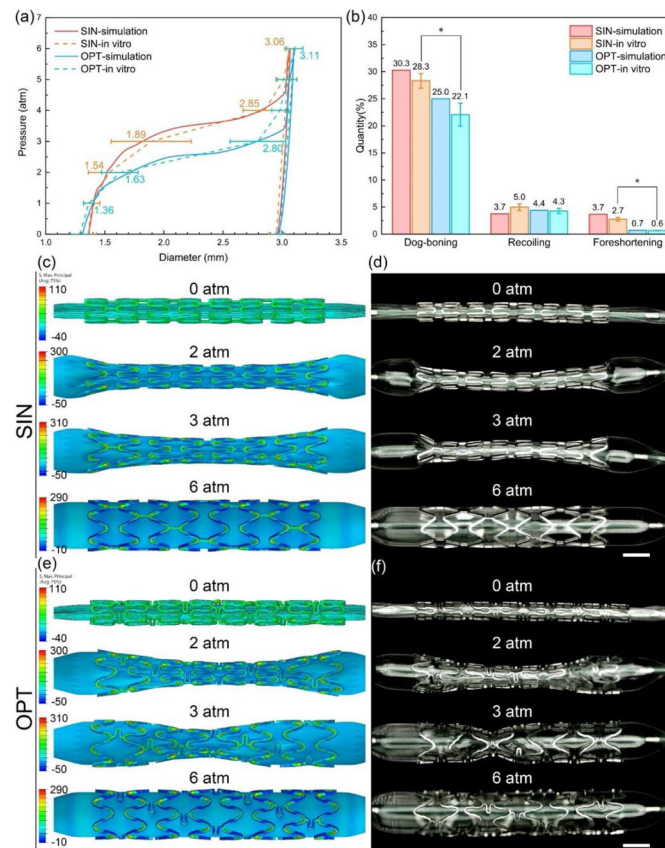
Figure 4.
Balloon expansion simulation of the SIN and the OPT stents with the corresponding validation experiments. (a) Pressure-diameter curves of stents from crimped status to a balloon pressure of 6 atm. (b) The dog-boning effect, recoiling in the radial direction and foreshortening in the axial direction of stents. *P< 0.05, n=5. (c, d) Simulated expansion (with maximum principal stress distribution) and experimental validation for SIN stent. (e, f) Simulated expansion (with maximum principal stress distribution) and experimental validation for OPT stent. Scale bars represent 1 mm.
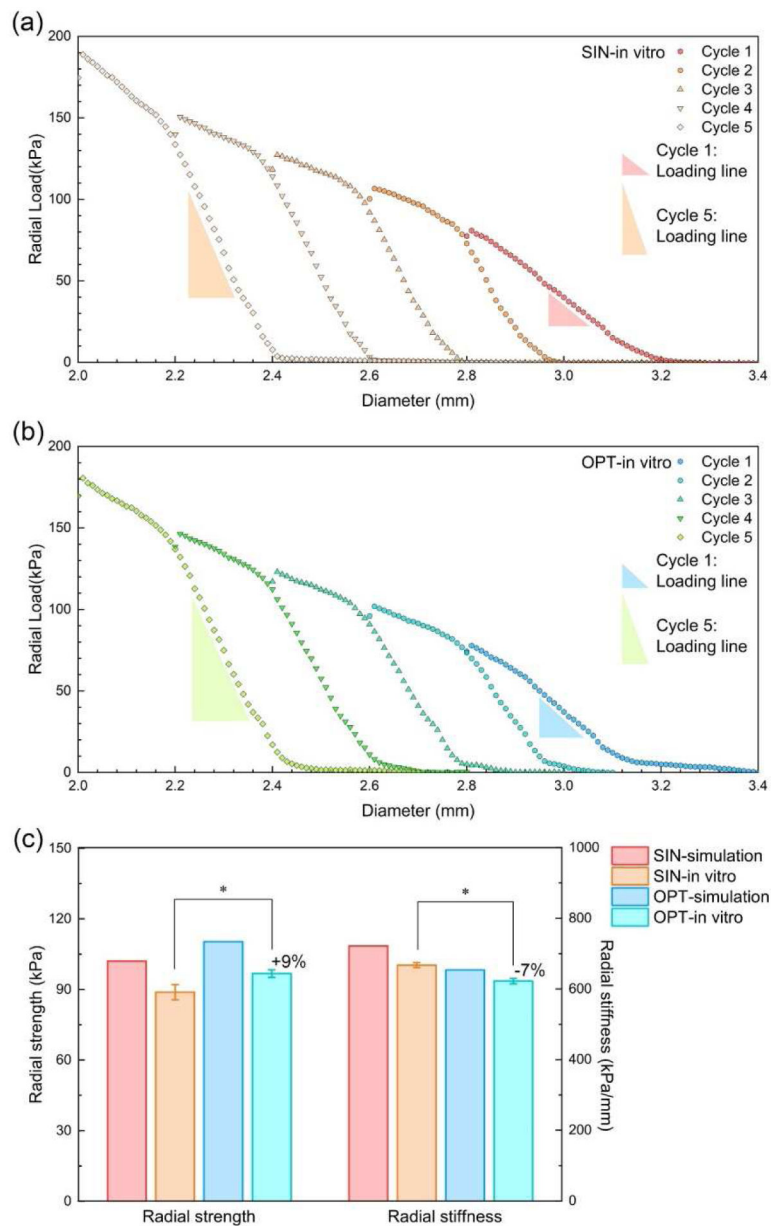
Figure 5.
The radial strength test of the SIN and OPT stents. The parallel loading lines for multi-cycles re-crimping tests of (a) the SIN and (b) OPT stents. The triangles marked the slopes of loading lines for cycle 1 and cycle 5, which were used for locating the initial contact point and measuring the radial stiffness respectively. (c) Result of radial strength and stiffness from simulations and experiment measurements. The radial strength of OPT stent is 9% higher than SIN stent and radial stiffness of OPT stent is 7% lower than SIN stent. $*P<$ 0.05, n=5.
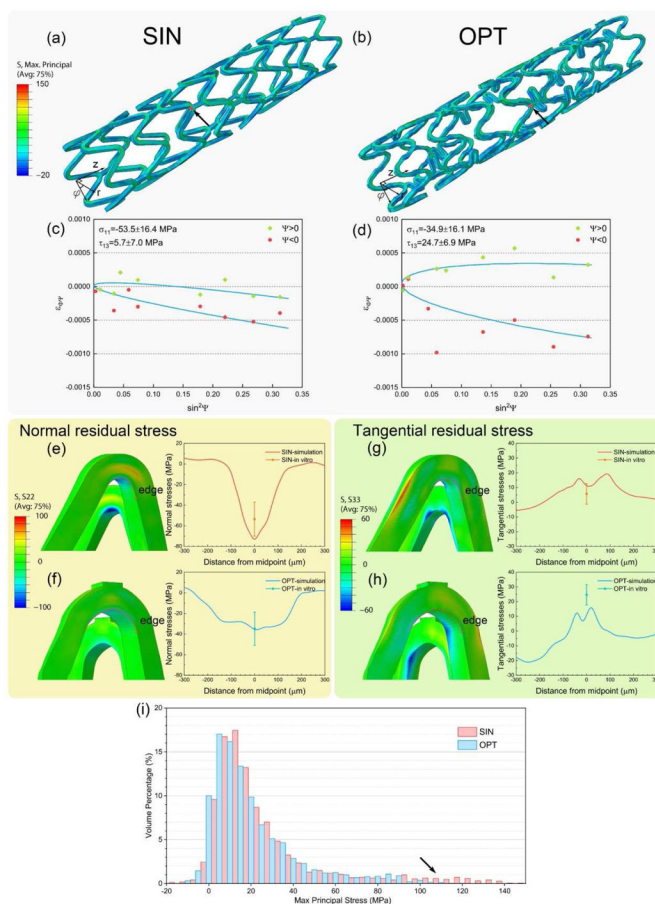
Figure 6.
The measurement and analysis of residual stress state. (a, b) The maximum principal stress distribution of the SIN and OPT stents after balloon inflation and recoil. The measured position of micro-area XRD were indicated by red points and black arrows. (c, d) The $\varepsilon_{\Phi\Psi} - sin^2\Psi$ diagram of {104} planes of magnesium on SIN and OPT stents. (e, f) The distribution of the circumferential stress component of the SIN and OPT stents. And the stress component values along the inner edge. (g, h) The distribution of axial stress component and the values along the inner edge for the SIN and OPT stents. (i) The histograms of the maximum principal stress of the SIN and OPT stents. The range of each bin is 5 MPa. Compared to the SIN stent, a significant reduction could be found in high-stress regions ($\geqslant$100 MPa) of the OPT stent, indicated by the black arrow.
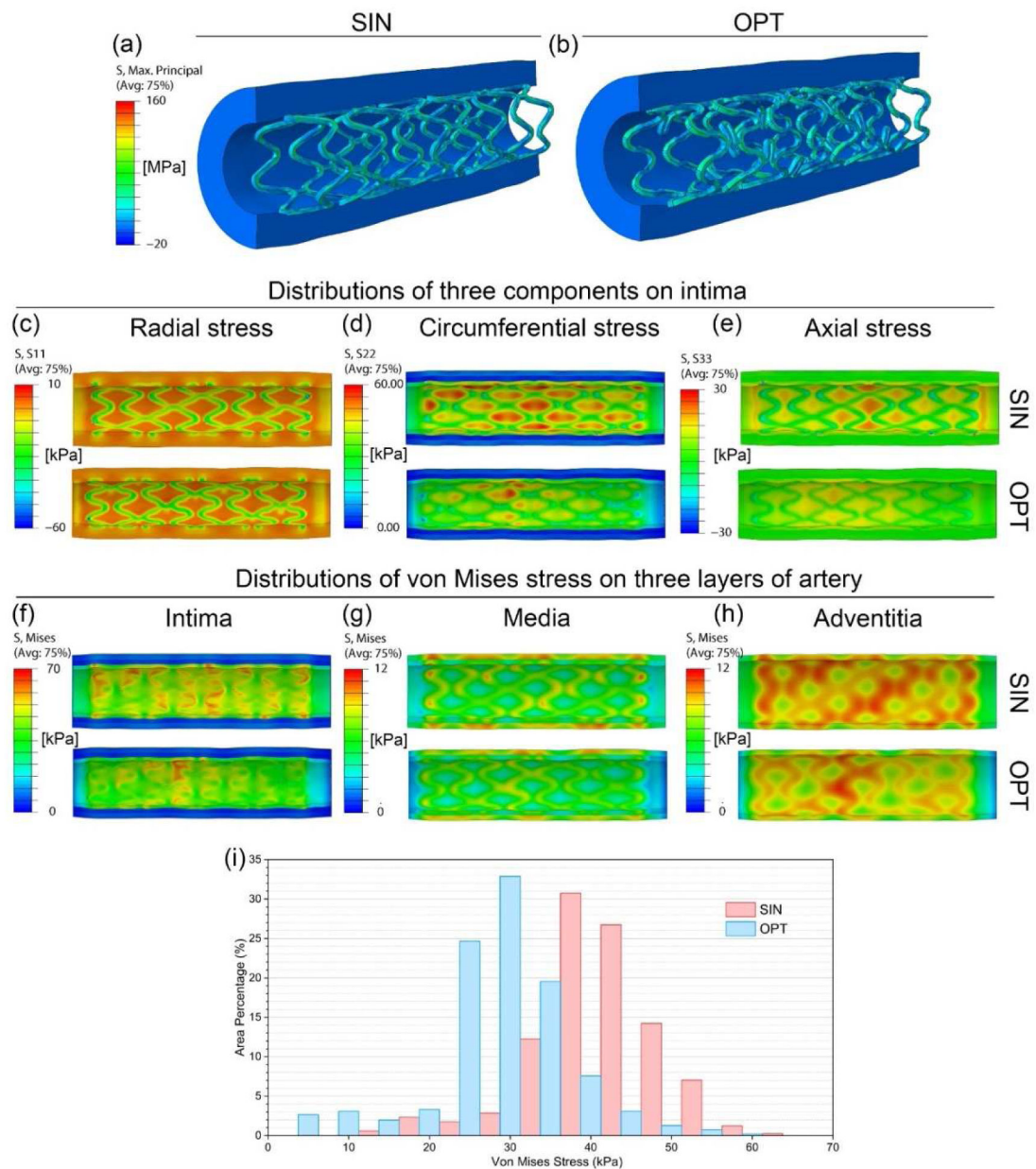
Figure 7.
Result of stents implantation in the vascular vessels. (a, b) Distributions of the maximum principal stress of the SIN and OPT stents. (c, d, e) Distributions of radial, circumferential and axial stress components in the stented region of the intima layer for the SIN (top) and OPT (bottom) stents. (f, g, h) Distributions of von Mises stress in the intima, media and adventitia layers for the SIN (top) and OPT (bottom) stents. (i) The histogram shows the area distribution of von Mises stress on the surfaces of the intima in the stented region for the SIN and OPT stents. The range of each bin is 5 MPa. Compared to the SIN stent, a significant reduction could be found in relative high-stress regions (≥40 kPa) of the OPT stent.
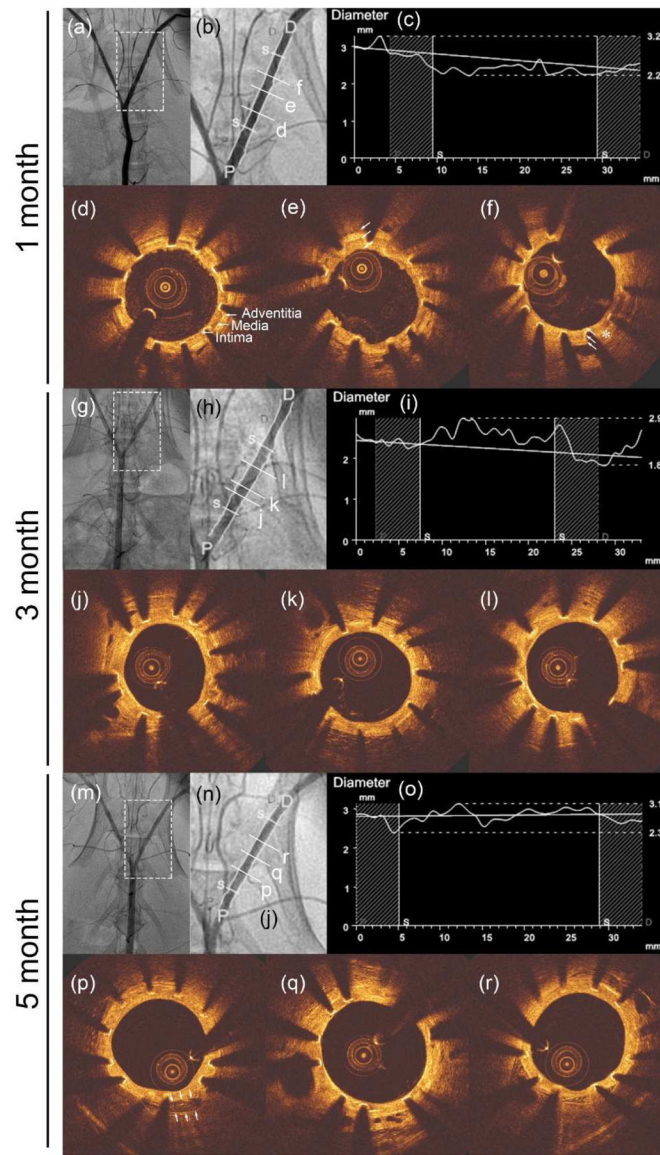
Figure 8.

In vivo observation and measurement via quantitative coronary angiography and optical coherence tomography. Upper panel shows the 1-month results. (a, b) Angiography in the rabbit and the location of the scaffolded-segment. (c) The distribution of the diameter along the iliac artery. (d, e, f) The OCT images in the scaffolded-segment. The bright-dark-bright 3-layered appearances corresponding to intima, media, and adventitia are indicated by the white arrows. The homogeneous, signal-rich regions corresponding to fibrous plaques are indicated by the asterisks. The middle and lower panels show the 3 and 5 months results respectively. The signal-poor region with sharply delineated borders corresponding to a calcific plaque is indicated by the double arrows.
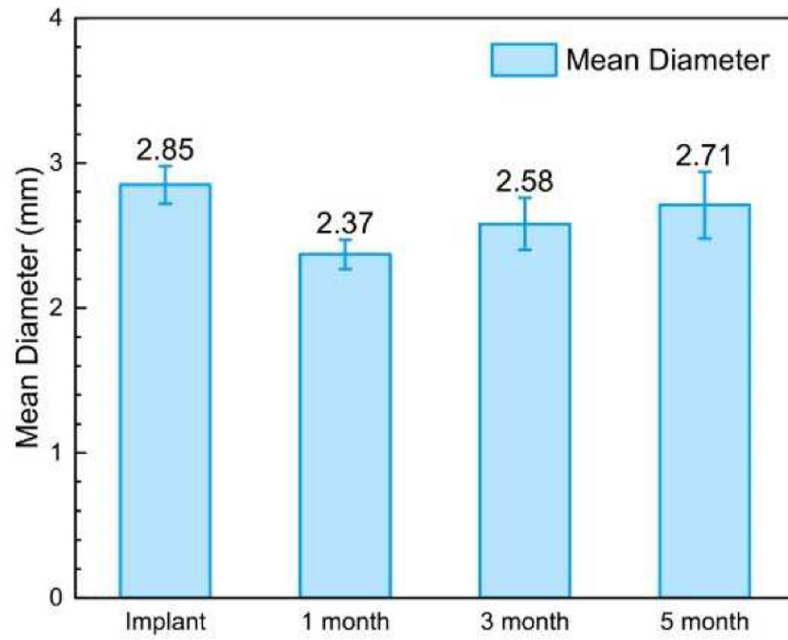
Figure 9.
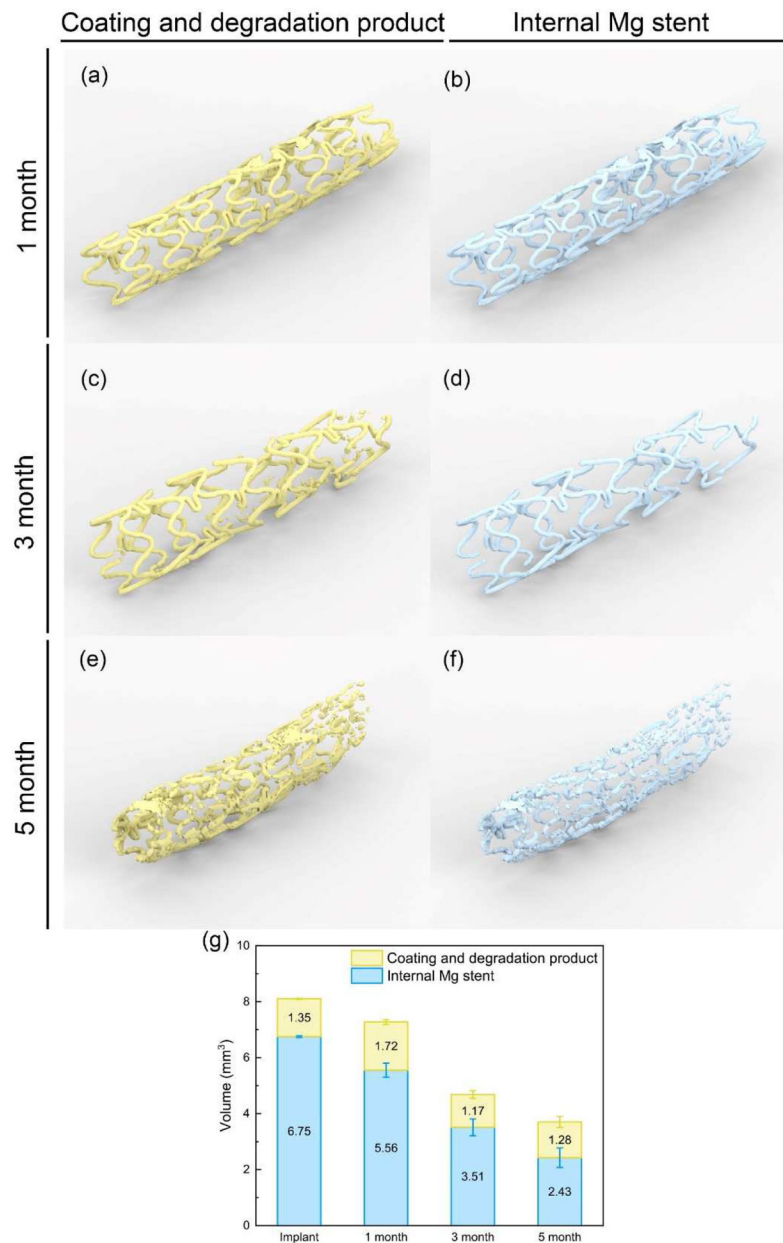The mean-diameters of scaffolded-segments at post-procedure of 1, 3 and 5 months.

Figure 10.
The reconstructed 3D models of coated OPT stent after 1, 3 and 5 months of implantation via high-resolution micro-CT. (a, b) No apparent degradation happened at 1 month after implantation. (c, d) Slight volume loss was found at 3 months. (e, f) OPT stent seriously degraded at 5 months. Due to the lower signal strength of magnesium stents and their degradation products than the permanent metal stent, slow scan speed and high X-ray intensity are recommended. (g) The volumes of internal magnesium stents, coatings and degradation products and calculated based on reconstructed 3D models.
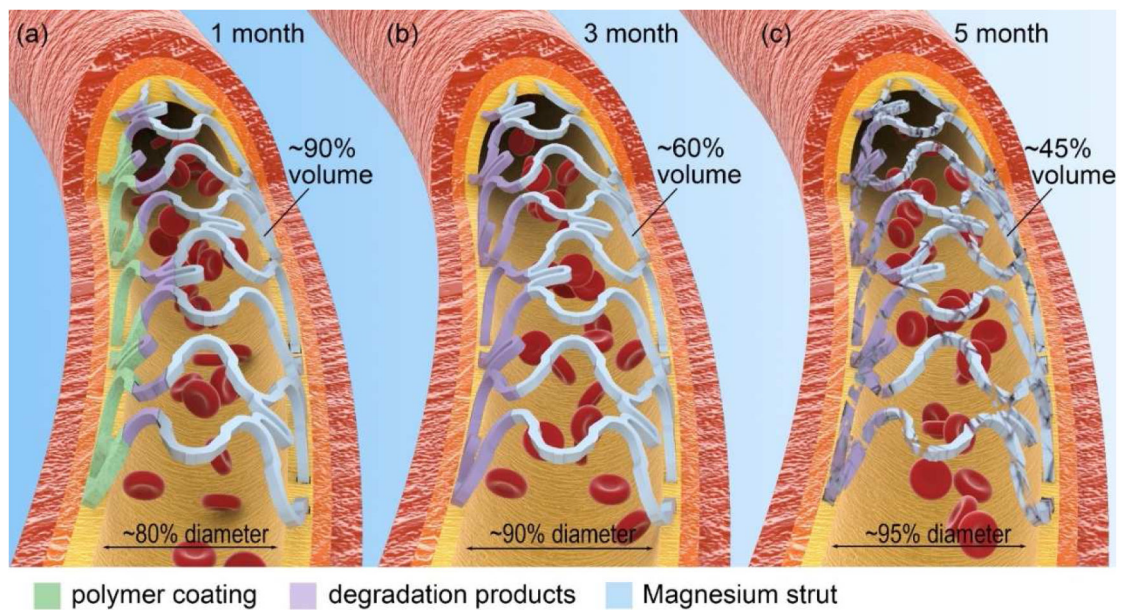
Figure 11.
Schema of stented-segments over time post-procedure. The left part of the stent in each panel shows the surface layer and right part the internal strut. Stents are compared with their initial volume, and the lumens are compared with the diameter post-implantation, (a) At 1 month follow up, degradation of Magnesium happened under the cover of polymer coating and vascular lining restored by complete endothelialization. (b) At the end of 3 months the major structures of the stent were still maintained supporting the vascular wall. While the polymer coating lost structure integrity and cannot provide effect protection for stent [51], (c) As the stent itself erodes over the next two months constraint on vasomotion is removed and vasoreactivity is restored.
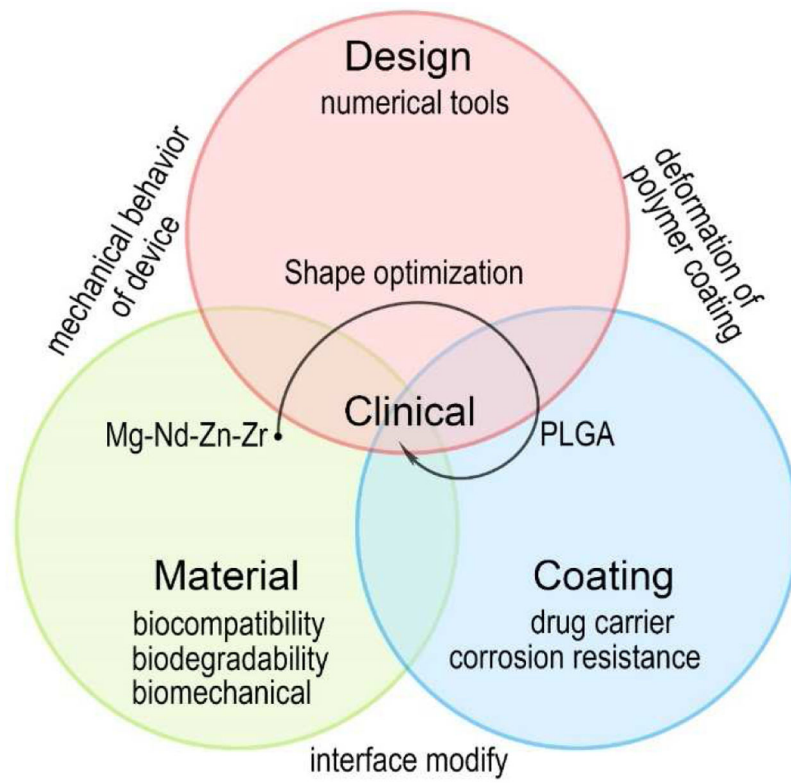
Figure 12.
Schematic diagram of the relationship among material, design and coating for BMgS.